PERGAMON

Journal of Structural Geology 22 (2000) 723–733

JOURNAL OF STRUCTURAL GEOLOGY

www.elsevier.nl/locate/jstrugeo

Microfracture pattern compared to core-scale fractures in the borehole of Soultz-sous-Forêts granite, Rhine graben, France

Chrystel Dezayes[a,b,*], Thierry Villemin[a], Arnaud Pêcher[c]

[a]*Laboratoire de Géodynamique des Chaînes Alpines, UPRES-A CNRS 5025, Université de Savoie, 73376 Le Bourget du Lac Cedex, France*
[b]*10 rue de Mortillet, 38000 Grenoble, France*
[c]*Laboratoire de Géodynamique des Chaînes Alpines, UPRES-A CNRS 5025, Université Joseph Fourier, Institut Dolomieu, 15 rue M. Gignoux, 38031 Grenoble, France*

Received 14 June 1999; accepted 13 January 2000

Abstract

Microfractures appearing in thin section as fluid inclusion trails in quartz crystals were studied in four core samples of Soultz-sous-Forêts granite. Their orientations in four series of three mutually perpendicular thin sections were estimated using a previously described apparent dip method and a new method involving measurements of strike and apparent dips.

Three samples display three microfracture sets and one sample displays two sets. In all samples, one set is nearly vertical and strikes N–S. In two samples, one and two sets are nearly vertical and strike E–W. In two samples, two sets strike NW–SE: one is vertical, the other dips gently to the NE (or SW). Comparing microfracture and mesofractures sets in the same cores shows that (1) the N–S microfracture set is always dominant at both scales and (2) all other microfracture sets have no mesoscopic counterpart. The N–S microfracture sets could have been created during E–W extension of earliest Cenozoic age (Rhine Graben rifting). Differences between the two scales are explained by a σ_1/σ_2 switching which occurred at the crystal scale and generated mutually perpendicular cracks.

1. Introduction

As fracture spacing is generally larger than core diameter, fracture sampling in the core is influenced by the orientation of the borehole (Terzaghi, 1965): thus fractures sub-parallel to the core are under-represented because they are unlikely to be intersected. This sampling problem can be corrected by using a weight function of the angle between each fracture and the core axis. Unfortunately this numerical correction introduces other sources of error, especially if the analysed core section is short. An alternative way to analyse the fracture consists of measuring fractures on a larger scale, such as in core samples and then extrapolating the results to other smaller scales. However, the same sampling problem applies to microfractures observed in a thin section, as fractures sub-parallel to the section will also be under-represented. Correcting this bias by applying a weight function of the angle between a fracture and the core axis or thin section introduces other sources of error because this assumes the fracture network to be homogeneous and that the studied thin section correctly samples the whole volume. To partly remove the bias, we have chosen to study the microfractures in each core sample by using three mutually perpendicular sections.

In this study of the Soultz-sous-Forêts granite (Fig. 1) we have analysed microfractures marked by fluid inclusion planes (FIP) in quartz crystals using the method of Lespinasse and Pêcher (1986). We also developed a new method of finding the orientation of FIP sets from only the strikes of trails. The aim of this paper is to describe this method, present the data, and to compare them with the mesoscopic data of Dezayes et al. (1995).

* Corresponding author.
E-mail address: chrystel.dezayes@univ-savoie.fr (C. Dezayes).

0191-8141/00/$ - see front matter
PII: S0191-8141(00)00003-1

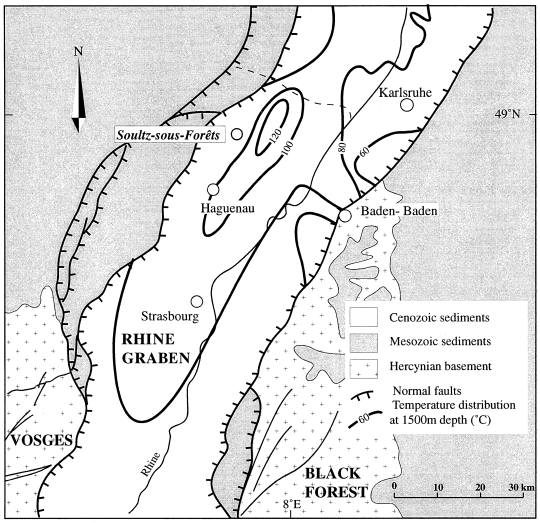

Fig. 1. Location of the Soultz-sous-Forêts geothermal site in the Rhine graben.

2. The Soultz-sous-Forêts geothermal site

Soultz-sous-Forêts is a Hot Dry Rock (HDR) geothermal site where a deep heat exchanger between two boreholes, 500 m apart, has been created by injecting cold water into one borehole and recovering hot water from the other (Gérard and Kappelmayer, 1987). The site is close to the western boundary fault of the Rhine graben and to a significant positive thermal anomaly near the old oil field of Pechelbronn (Fig. 1). The temperature is about 160°C at a depth of 3700 m. Seismic profiles reveal tilted blocks in the sedimentary cover of Cenozoic infill and Triassic pre-rift strata (Brun et al., 1991). A horst in the basement has resulted in the granite being encountered at a depth of 1400 m.

The geothermal reservoir is Visean porphyritic granite (Kölher, 1989) that contains K-feldspar megacrystals associated with quartz, plagioclase, biotite, hornblende and secondary apatite, titanite and magnetite (Genter and Traineau, 1992). The rock is homogeneous except locally, where biotite and hornblende have been pervasively altered to chlorite (Genter, 1989).

Of the three deep boreholes drilled for the HDR project, GPK1 was not cored to a depth of 3570 m, EPS1 encountered the granite at a depth of 1417 m and was fully cored from 933 to 2227 m (Fig. 2), and GPK2 was drilled without core to a depth of 3880 m. The data presented in this paper come from four EPS1 granitic core samples from depths of 1419, 1624, 2055 and 2179 m (Fig. 2).

Knowledge of the fracture pattern is one of the most important parameters needed to study fluid circulation in such a reservoir rock with low permeability.

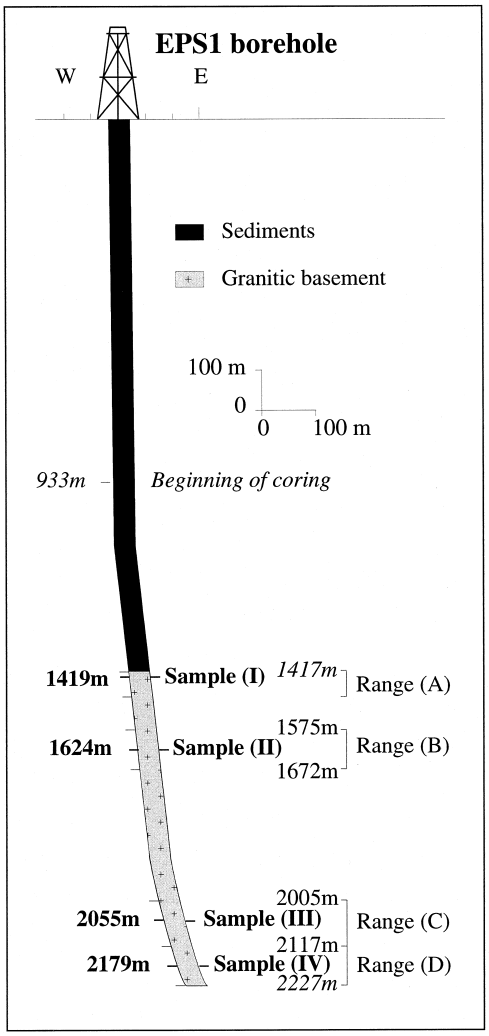

Fig. 2. E–W view of EPS1 borehole showing the locations of core samples I–IV used for thin sections and the depth ranges of the four groups of macrofractures.

Fractures on all scales contribute to permeability and must be taken into account, especially if the rock was subjected to fluid injection. In addition, a microfracture study completes the information given at a mesoscopic scale if scale invariance is observed.

3. Microfracture features

Microfractures in this study are microcracks outlined by fluid inclusion trails (Fig. 3) corresponding to FIP. These trails occur in most minerals but the absence of cleavage makes detecting them easiest in quartz. In the Soultz granite, quartz crystals are xenomorphic and average 5 mm across, and the trails range from about 0.1 mm to 15 mm long. Microcavities (Fig. 3) are filled with primary fluids when formed during crystal growth (Clocchiatti,

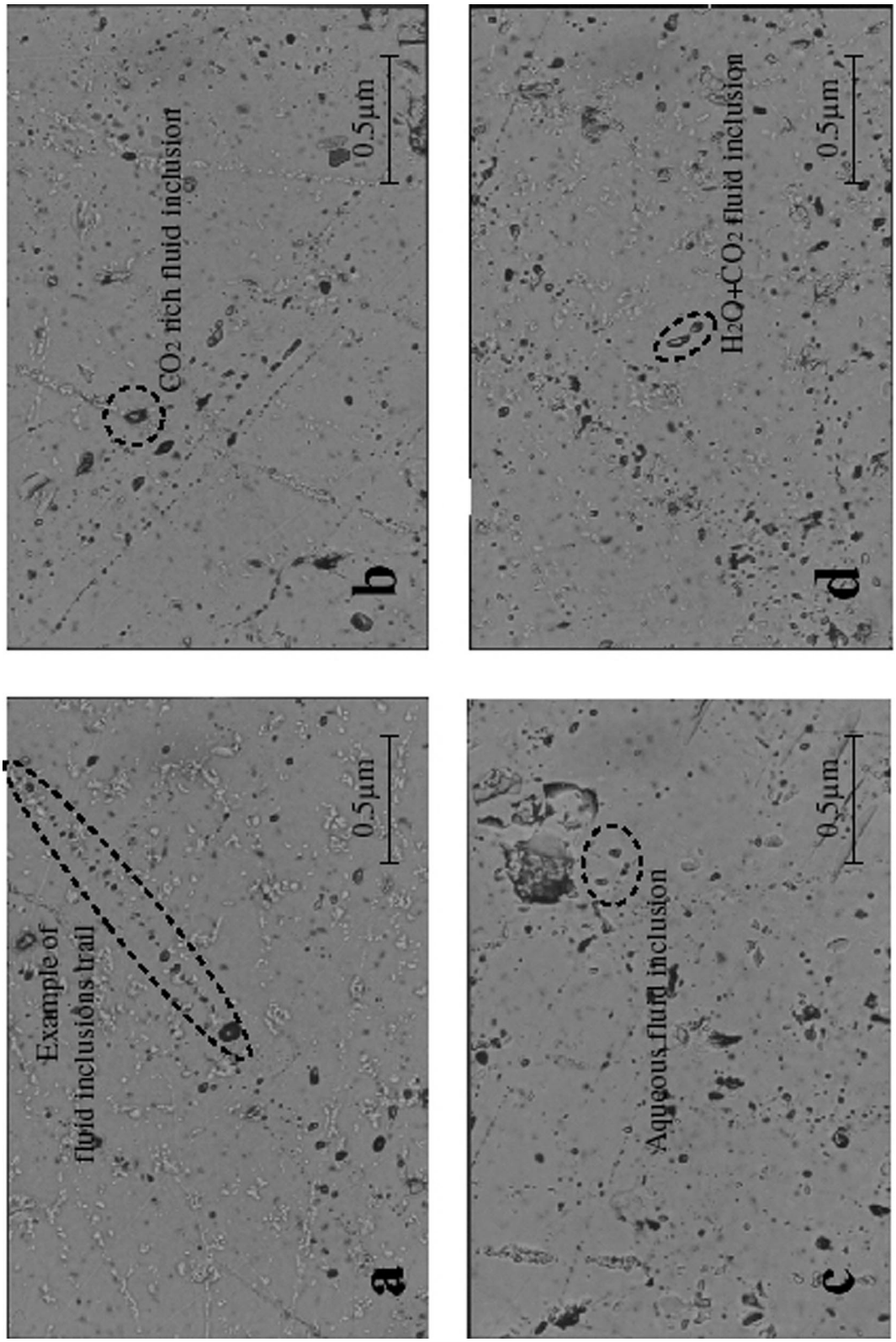

Fig. 3. Fluid inclusions in quartz. (a) The trace of a fluid inclusion plane. (b) CO_2 rich fluid inclusion. (c) Aqueous fluid inclusion. (d) H_2O+CO_2 fluid inclusion.

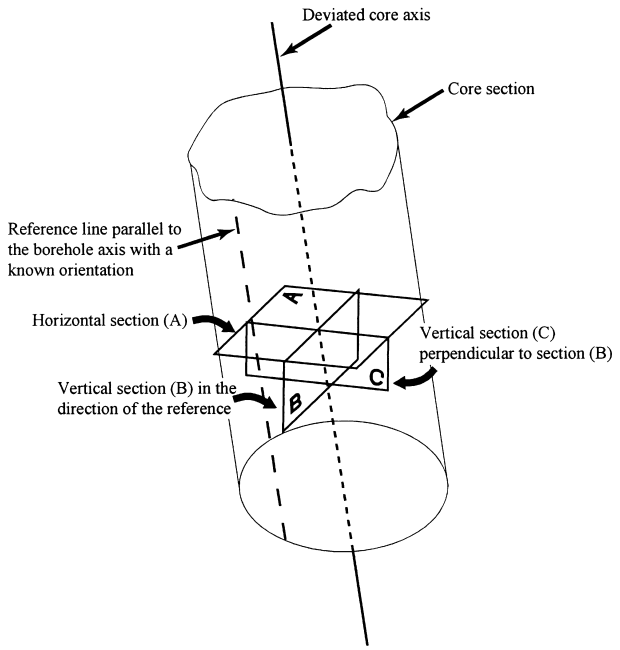

Fig. 4. Cutting convention for thin sections in cores from a deviated borehole. Section B has the same direction as the reference and section C is perpendicular to it.

1975; Roedder, 1979; Hollister and Crawford, 1981; Lespinasse and Pêcher, 1986) or with secondary fluids if they occur in sealed cracks. Only the latter were observed in the Soultz granite. Sealed crack FIP are usually interpreted as mode I cracks (Lespinasse and Pêcher, 1986) reflecting the stress state during crack opening: the fracture planes are perpendicular to the minimum principal stress axis σ_3. Although such sealed cracks are discontinuous, they introduce weakness zones in crystals.

Fluid inclusions at Soultz have previously been studied only from a geochemical point of view and only in altered parts of the cores (Dubois et al., 1996; Ledésert, 1995). In our study, FIP have been analysed only in unaltered parts of the granite and only in thin section. To eliminate bias in estimating the orientations of microfractures, three mutually perpendicular thin sections were made from each sample. As the drillhole is more or less vertical (Fig. 2) and as we had no prior information on preferred orientations we decided to make one thin section horizontal taking into account the deviation of the borehole (Fig. 4, A) and the other two vertical (Fig. 4, B and C).

4. Measuring orientation from apparent dip

To test a new method for estimating the orientation of an FIP, the 'apparent dip' method of Lespinasse and Pêcher (1986) was applied to samples I and III (Fig. 2). This involved measuring the apparent strike α and apparent dip β in the plane of section. Whereas α can be measured directly ($\pm 6^\circ$), β had to be computed from the lateral displacement e of the trail's trace when moving the focused plane [Eq. (1) and Fig. 5]. The thin-section thickness estimated from a reference thickness is 28.8 μm ± 0.1 for all sections. The measurement accuracy is estimated as two graduations on the microscope, which implies an error of 4 μm on e and $\pm 5^\circ$ on β.

$$\beta = \arctan\left(\frac{t}{e}\right) \tag{1}$$

On horizontal thin sections α gives the strike of the FIP and β its dip. On vertical sections the orientation was found by solving three simultaneous equations in (L, M, N), the direction cosines of the normal to the FIP (Figs. 5 and 6). The intersection I (Fig. 6) between the FIP and the thin section is a line of plunge α, whose trend is deduced from the orientation of the thin section (Fig. 6), and whose direction cosines (l_1, m_1, n_1) are therefore given by Eq. (2). The other two equations used to find (L, M, N) are Eqs. (3) and (4), where (l_2, m_2, 0) are the direction cosines of the normal to the vertical thin section. Eqs. (2), (3) and (4) have two solutions, F_1 and F_2, symmetrical about the thin section (Fig. 6). The sense of dip of the FIP in thin section enables the correct solution to be selected.

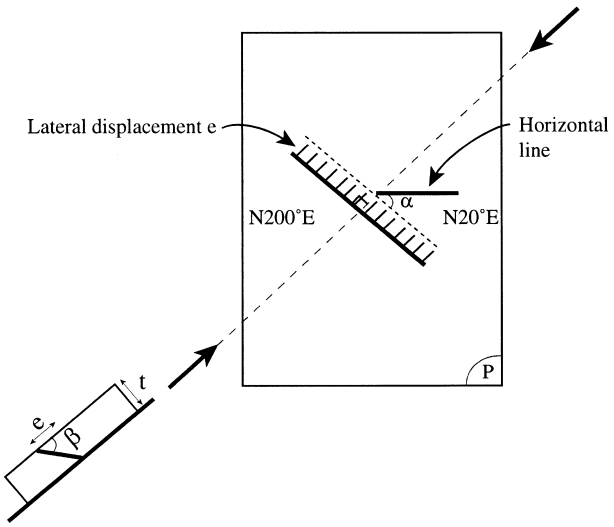

Fig. 5. Measurements on vertical thin sections (B and C). With a microscope, its cross hairs and universal stage, we can measure the apparent strike α of an FIP trail directly. The apparent dip β can be found from the thickness t of the thin section and the lateral displacement e of the trail's trace when moving the focused plane. P is the thin section plane. Arrows indicate cross-section perpendicular to the trace.

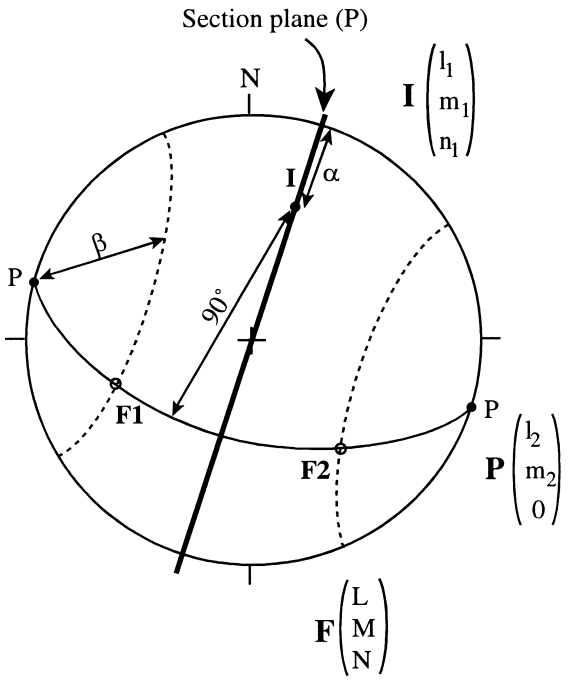

Fig. 6. Stereogram illustrating the graphical and numerical determination of F_1 and F_2, the two possible orientations of an FIP pole, from the FIPs apparent strike α (labelled α) and apparent dip β (labelled β) in a vertical cross-section. Graphically, F_1 and F_2 lie at the intersections of (1) the great circle representing the plane perpendicular to the intersection I of the section plane P (bold) and the FIP and (2) the cone represented by two small circles whose semi-apical angle is β and whose axis is the pole of section plane P. The numerical solution is described in the text. The choice between F_1 and F_2 is made using the sense of dip of the FIP in the thin section (Fig. 5).

$$l_1L + m_1M + n_1N = 0 \quad (2)$$

$$l_2L + m_2M = \cos\beta \quad (3)$$

$$L^2 + M^2 + N^2 = 1. \quad (4)$$

We made 60 measurements on each of the three thin sections for samples I and III. The number of measurements was chosen arbitrarily and the FIP were randomly selected. The orientations are displayed in Fig. 7. Density contour values were computed (i) using the same number of measurement for all sections (60 randomly chosen data per thin section, Fig. 7, column B) and (ii) taking into account fracture densities on each thin section (Fig. 7, column C). We analysed only samples I and III (Fig. 2) in this way because it has been performed only in order to validate the new method presented below. Fractures are distributed in three sets calculated with an algorithm of automatic classification. These three sets correspond to the three contouring maxima (Fig. 7). We computed the best plane for these sets assuming a Watson circular distribution (Table 1; Fisher et al., 1987). The small semi-vertical angles of the 95% and 99% confidences cones have been obtained and show that the position of maximum are well defined.

5. Measuring orientations from strike and apparent dip

Although the orientation of a FIP can be measured directly using a universal stage microscope, FIP are too numerous in our thin sections for all of them to be measured in this way. Consequently, 63 randomly distributed images from the 12 thin sections were acquired by a 3-CCD colour camera and then digitised as pixel images. Each enlarged image represents only 7 mm^2 of a thin section. As a first step we identified FIP in thin section, marked the traces on the images and then digitised them. Later the azimuth and length of each trace were measured automatically. For FIP made of different segments with variable orientation (deviation of more than 10% from the previous segment orientation), we measured separately the direction of each segments. We never observed 'en échelon' cracks. Altogether 4650 traces were measured.

In horizontal sections, the azimuth gives the strike of FIP (Figs. 8 and 1). In a vertical section, the azimuth corresponds to apparent dip in a direction parallel to the strike of section. These measurements are displayed on rose diagrams (Figs. 8, 2 and 3). We computed confidence intervals for the maximal peak on the rose diagram 1 and 2 (Fig. 8) assuming a symmetric unimodal Von Mises distribution (Table 2; Fisher et al., 1987). The relatively small values obtained for the confidence intervals show that the position of the preferred orientations are again quite well defined. Each peak on a rose histogram corresponds to a line whose orientation is known. All lines have been plotted on a stereogram (Fig. 8). Each FIP has to contain one line from each of the three mutually perpendicular sections. For example peak A-1 from Fig. 8(A) can be associated with peaks on the corresponding vertical sections in only three ways (A-1 B-3 C-6, A-1 B-1 C-4, A-1 B-2 C-3) as all other combinations are not geometrically compatible. Each peak on a rose diagram has been assigned a number giving its relative importance. To choose between two or more possible solutions, we tried to associate each FIP with peaks of similar importance; e.g. (A-1, B-1, C-4) is preferable to (A-1, B-3, C-6). We also tried to take into account the fact that a vertical section subparallel to an FIP is unlikely to cut it, so the FIP is likely to be represented on that section by a relatively unimportant peak. For example, the strike of the FIP containing peak A-1 in Figs. 8 and 1 is close to the strike of section C and more or less perpendicular to that of

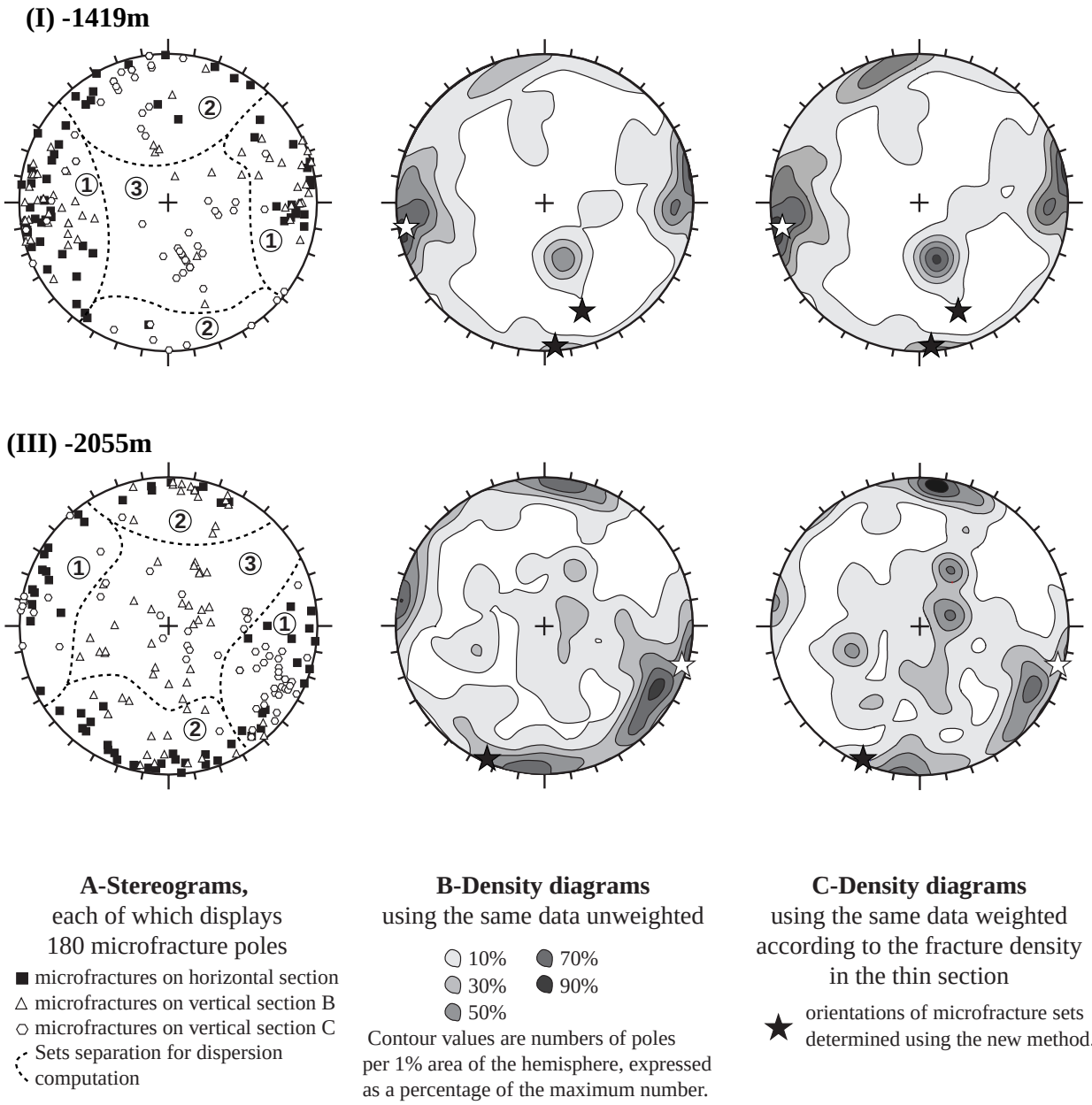

Fig. 7. Orientation diagrams for microfractures in samples I and III determined using the apparent dip method. For each sample, 60 orientations were measured in each of three mutually perpendicular thin sections. A—Stereograms displaying individual orientations. B—Contoured stereograms using the same data, unweighted. C—Contoured stereograms using the same data weighted by the fracture density on each section.

Table 1
Confidence cones for the TIF distribution. Best planes are computed for the three sets of the TIF distribution shown in Fig. 7. Semi-vertical angles of the 95% and 99% confidence cones are computed assuming a Watson type distribution

Fig. 7	Sets	Number of data	Best plane	Confidence cone for	
			Azimuth, dip, dip direction	95%	99%
Sample I	1	106	175°/84°E	4.6°	5.8°
–1419 m	2	45	081°/76°S	8.0°	10.0°
	3	29	059/28°N	7.4°	9.1°
Sample III	1	74	023°/82°N	5.4°	6.7°
–2055 m	2	62	098°/85N	6.1°	7.6°
	3	44	150°/04°W	10.3°	12.9°

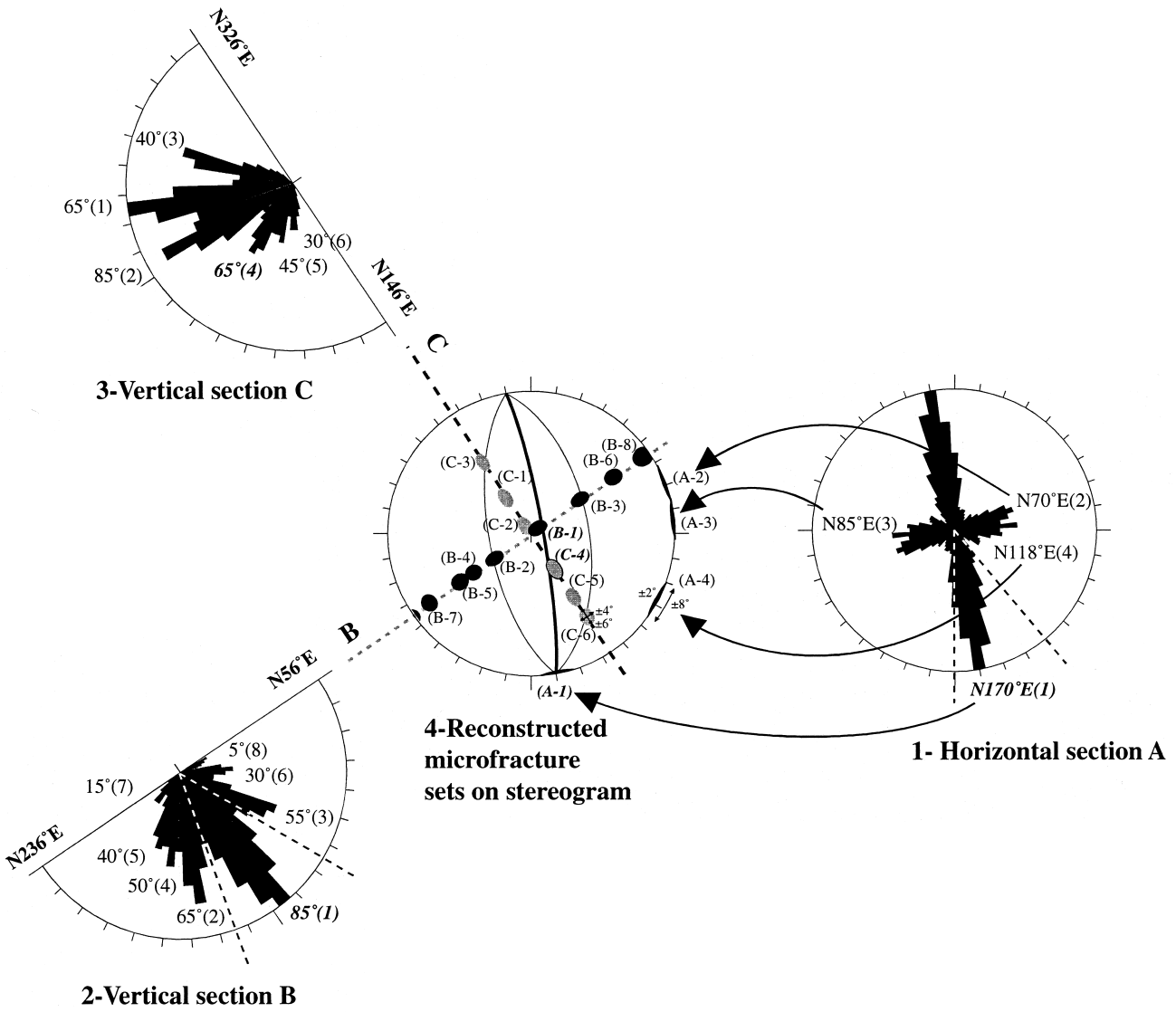

Fig. 8. Determination of FIP sets for sample I. For each thin section, azimuths are displayed on rose diagrams whose radius corresponds to the greatest frequency. In horizontal sections, azimuth gives the strike of FIP (1), whereas in vertical sections (2 and 3) it gives the apparent dip in a plane parallel to section strike. Peaks on (1) give the strikes and on (2) and (3) the apparent dips of FIP sets whose relative importance is indicated by the numbers in brackets. Each peak represents a line in 3D space whose orientation was found from its azimuth and the section orientation. These lines are plotted on the stereogram (4). Each FIP set is associated with a line from each of the sections. The FIP containing A-1 has three possible orientations of which the one in bold is the most likely (see text).

Table 2
Confidence angles for azimuth and apparent dip TIF. Confidence semi-angles are computed for the largest peak of the rose diagrams 1 and 2 shown in Fig. 8, assuming a Von Mises type distribution. k: concentration parameter (the high values found here indicate a very strong concentration of the values around the maximum)

Fig. 8	Peak	Number of data	Coefficient	Confidence angle for	
			k	95%	99%
Rose diagram 1 horizontal section A	N140° to N180° (40°)	251	38.93	1.1°	1.5°
Rose diagram 2 vertical section B	75° (plunge to N236°) 65° (plunge to N56°)	128	27.88	1.9°	2.5°

section B (Figs. 8 and 4), so we preferred the (A-1, B-1, C-4) solution to (A-1, B-2, C-3). The plane reconstructed from these three average lines has a dip direction of 80° and a dip of 83° (80°; 83°). The same notation (dip direction from 0° to 360°, dip from 0° to 90°) will be used below.

Fig. 9 summarises the rose diagram data and the microfracture set orientations deduced from this method. Each rose diagram displays two or three major peaks. For the purposes of the following discussion, we restricted our geometrical reconstruction to the two or three major peaks observed in horizontal sections (Fig. 9, column 1). The orientation of the microfracture sets deduced from this method are in Table 3.

To test the validity of this new method we compared the results given by the apparent dip method. Fig. 7 (columns B and C) shows the mean poles given by the new method and those obtained from the density diagrams given by the apparent dip method. Each average FIP plane, geometrically reconstructed, corresponds to an area of high density directly measured poles and vice versa. As the small remaining differences are negligible, we can confirm the validity of the method.

6. Orientations of microfracture sets

Sample I (Fig. 9, row I). In section A the dominant peak strikes N170°E with most other data restricted to a 20° range about N80°E. Apparent dips in section B suggest three peaks, one ranging from 50° to 70°E, another from 50° to 70° W, and one vertical. In section C, apparent dips also reveal three peaks. Making the assumptions referred to above, three FIP sets appear to be present: (a) 80°/83°, (b) 340°/66° and (c) 355°/87° (Fig. 9 I-4).

Sample II (Fig. 9, row II). In section A, the dominant peak strikes N25°E with most other data

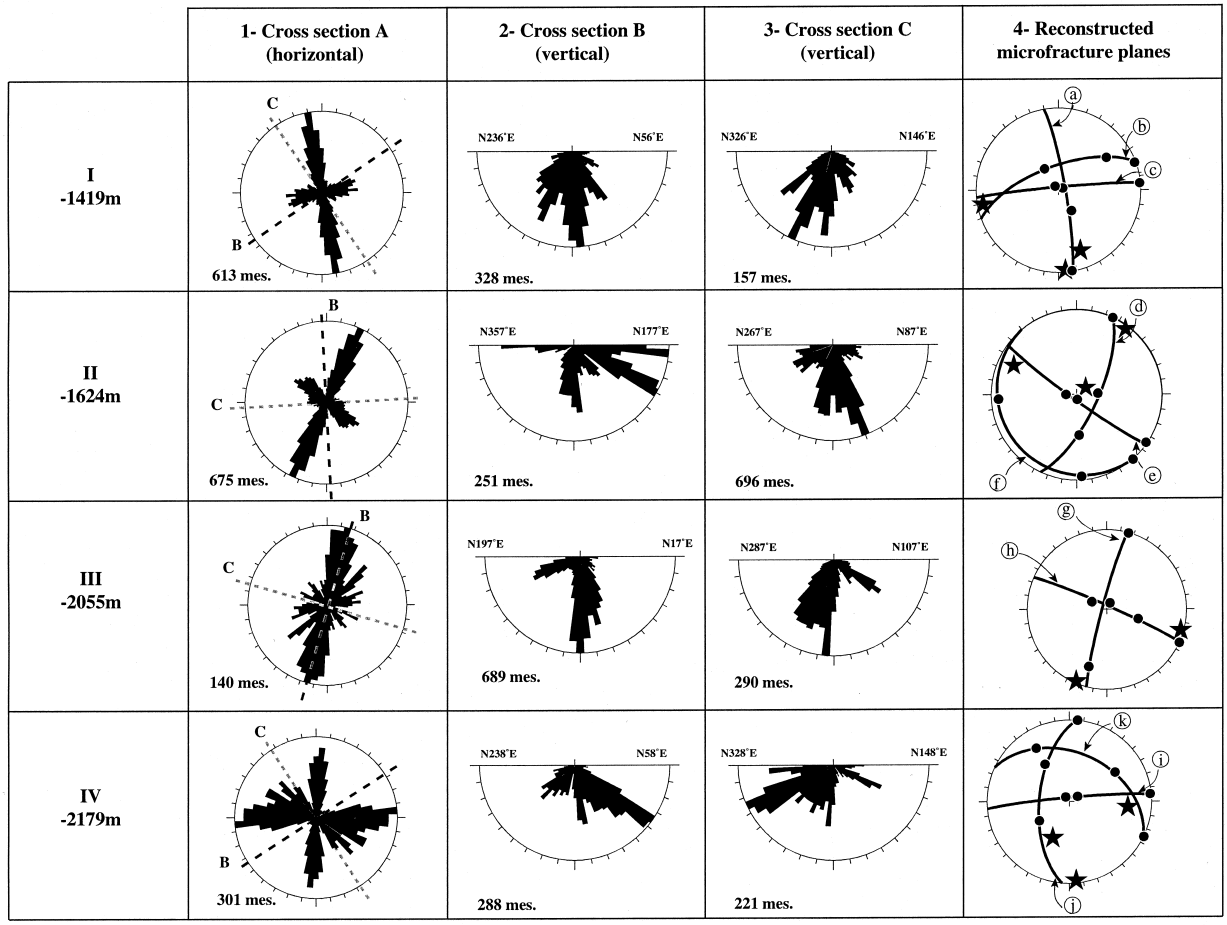

Fig. 9. Strikes and apparent dips of fluid inclusion trails and reconstructed FIP sets. Rose diagrams showing the strikes (1) and apparent dips (2 and 3) of fluid inclusion trails and stereograms showing the FIP sets found from analysing these data (4), for samples I–IV. The rose diagrams are scaled so that the radius corresponds to the size of the largest class. In the stereograms, great circles represent FIP and stars their poles, and the circular symbols represent peaks on rose diagrams used to find FIP orientations.

restricted to a 20° range about N125°E. Data are very scattered on section B but we can see three peaks, one horizontal, one at 30° S and one vertical. On section C, peaks occur at about 80° E and 70° W and many traces have apparent dips less than 30°. Three FIP sets are suggested: (d) 115°/70°, (e) 216°/85° and (f) 230°/10°.

Sample III (Fig. 9, row III). On section A the dominant strike is N15°E. Most traces peak at 70° to 90° on sections B and C. A second peak at 20°S is visible on section B and at 30°E on section C. Only two FIP sets are suggested by the data. Only one geometrically compatible association can be drawn with peak dipping 25°S in section B and with peak dipping 85°W in section C, giving the plane (g) 285°/86°. The second set is (h) 25°/80°.

Sample IV (Fig. 9, row IV). Although there is much scatter, on section A two major strikes at N5°E and N85°E can be distinguished. The vertical rose diagrams each have three peaks. Apparent dips are mainly between 20° and 50° NE for section B and between 20° and 40°NW for section C. These data suggest the existence of FIP sets (i) 355°/85°, (j) 275°/65° and (k) 25°/40°.

In summary, three samples display three FIP sets and one sample displays two sets (Figs. 9 and 4). In all samples, one of them strikes nearly N–S and dips 70–90° in samples I, II and III and 65°N in sample IV (Figs. 8 and 4). In samples I and IV, a vertical set strikes nearly E–W (Figs. 9 and 4, planes c and i). In samples II and III, another vertical set strikes NW–SE. In each sample, two sets are at least more or less mutually perpendicular.

Table 3
Orientation values of FIP sets determinate by 3D reconstruction. Orientations are dip direction and dip

Samples Depth (m)	FIP sets	Plane Dip direction/Dip	Pole Dip direction/Dip
I-1419 m	a	080°/83°	260°/07°
	b	340°/66°	160°/24°
	c	355°/87°	175°/03°
II-1624 m	d	115°/70°	295°/20°
	e	216°/85°	036°/05°
	f	230°/10°	050°/80°
III-2055 m	g	285°/86°	105°/06°
	h	025°/80°	205°/10°
IV-2179 m	i	355°/85°	175°/05°
	j	275°/65°	095°/25°
	k	025°/40°	225°/50°

7. Relationship between micro- and mesofractures

About 3700 mesoscopic fractures along the entire granitic core section were measured and oriented by comparison with BHTV borehole images (Borehole Televiewer) (Genter and Traineau, 1992). To compare these fractures with our data, we divided the former into four groups of 50 m deep around the four depths of our samples (Fig. 2): A-1417 to 1469 m, B-1575 to 1672 m, C-2005 to 2117 m, and D-2117 to 2227 m.

In group A (range A, Fig. 2), although the mesofracture poles are distributed mainly around the 255°/15° axis, which is close to the average pole of microfracture set (a) 260°/7°, secondary microfracture sets (b) 160°/24° and (c) 175°/3° have no mesoscopic counterpart (Fig. 10A).

In group B (range B, Fig. 2), although the main microfracture set (d) (295°/20°) correlates well with the major mesofracture set, microfracture sets (e) 36°/5° and (f) 50°/80° do not correspond with any mesofracture set (Fig. 10B).

In group C (range C, Fig. 2), although mesofracture poles cluster around the 95°/10° axis, which agrees well with FIP pole (g) 105°/6°, microfracture set (h) 205°/10° cannot be correlated with any mesofracture set (Fig. 10C).

In group D (range D, Fig. 2), two mesofracture sets are present with orientations of 90°/15° and 125°/15° (Fig. 10C). Microfracture set (j) 95°/25° correlates well with the first mesofracture set. Conversely, microfracture sets (i) and (k) whose average poles are respectively oriented 175°/5° and 205°/50° have no mesoscopic counterpart.

In conclusion, the N-striking microfracture sets correlate well with the main mesofracture sets but the other microfracture sets have no mesoscopic counterparts. The N-striking microfracture sets are dominant in all samples except IV where, however, it remains significant.

8. Discussion

In our four samples we found one or two microfracture sets that cannot be recognised at the scale of the core. In one case (set f, Fig. 10), the microfracture set is perpendicular to the borehole. Since fractures of this orientation are the most likely to be intersected, the fact that they were not detected by the mesoscopic analysis means they really do not exist at this scale. The situation is different for inclined sets (b) and (k) (Fig. 10), but the conclusions are similar because these sets are in the lowest density area for mesoscopic fractures. Sets (c), (e), (h) and (i) (Fig. 10) correspond to more or less vertical fractures. For these cases, we cannot conclude with certainty that similar orientations

are absent at a mesoscopic scale because such fractures with these orientations are unlikely to be intersected by a vertical well. We believe that (c), (e), (h) and (i) are not present at a large frequency at the mesoscopic scale. The reasons for that are that the fractures are scattered around these average orientations and that EPS1 borehole is a little deviated as shown on Fig. 2. Therefore there is a real difference between microfracture mesoscopic patterns. Some families present on one scale are not significant on another.

The origin of mesoscopic fracturing is discussed in detail in Dezayes et al. (1995). As microfractures associated with poles (a), (d), (g) and (j) have mesoscopic counterparts, we assume that they have similar origins and developed during Oligocene rifting. Sets (c), (e), and (h) are more or less perpendicular respectively to sets (a), (d) and (g) and cannot be related to any state of stress reconstructed by Dezayes et al. (1995) for the Soultz granite and Villemin (1986) at a regional scale. For these reasons, we propose that a mechanical stress σ_1/σ_2 switching occurred at a grain scale and was responsible for both E–W vertical microfracture sets (c), (e) and (h) and N–S vertical sets (a), (d) and (g). Such an explanation has already been used to explain similar data (Angelier and Bergerat, 1983).

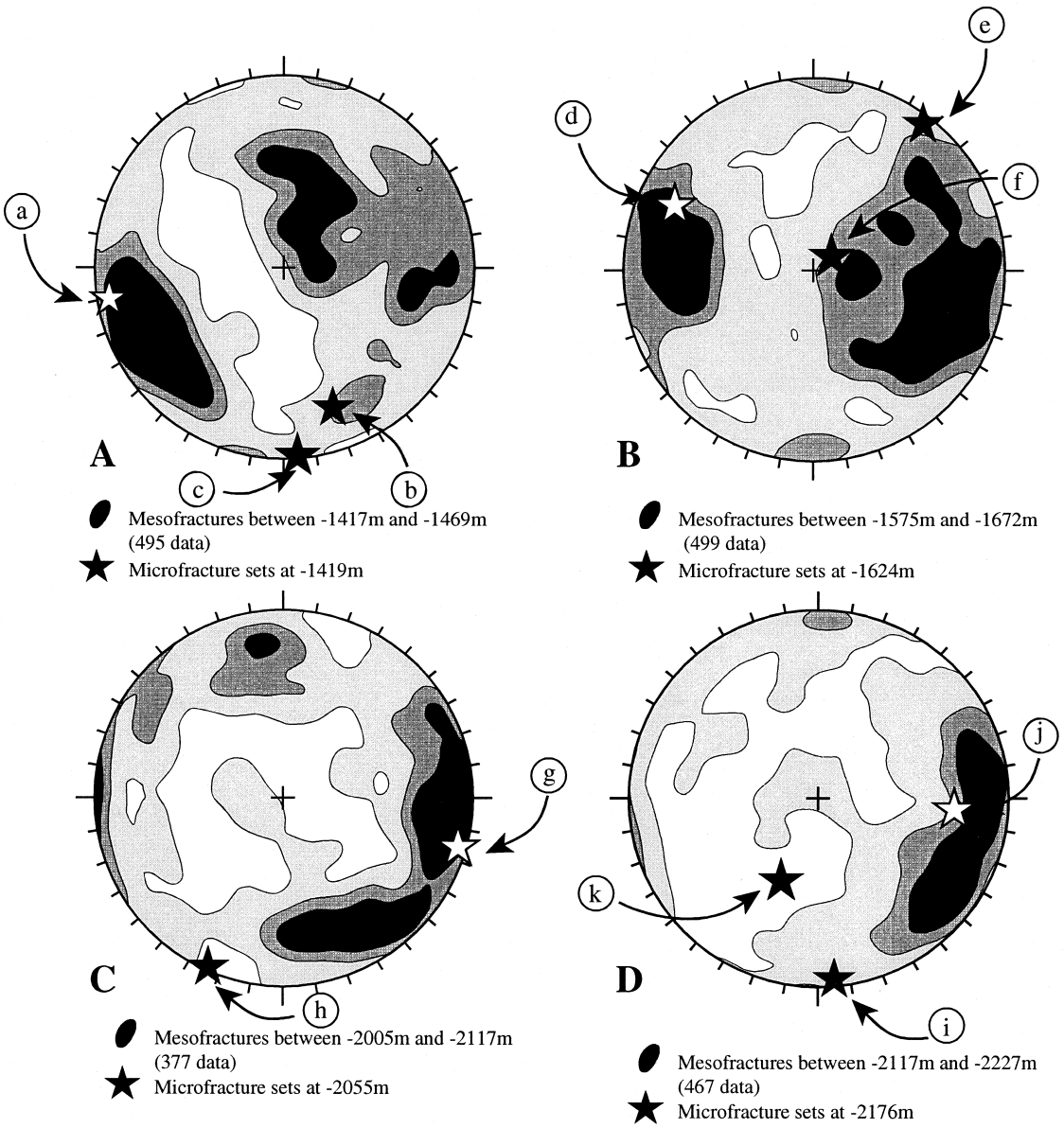

Fig. 10. Comparison between micro- and mesofracturation. Contoured density diagrams of four groups of mesofractures from borehole EPS1 whose depth ranges are shown in Fig. 2 (see Fig. 7 for contour values). Superposed on these diagrams are the poles of FIP sets (stars). Only the N-striking FIP sets correlate well with the major mesofracture sets. The other FIP sets have no mesoscopic counterparts.

9. Conclusions

To determine the orientation of microfractures we have applied two methods, both of which used three mutually perpendicular thin sections to eliminate sampling problems associated with section orientation. The apparent dip method of Lespinasse and Pêcher (1986) was used to validate the second method, which is new. The main advantage of the new procedure is that it is based only on strike measurements that can be made automatically from numerical images. Also, many data can be taken into account at the same time and the principal orientation sets can be measured accurately.

The FIP set orientations have been compared with those of mesoscopic fractures observed in borehole cores. Most mesofractures resulted from the Cenozoic rifting in the area (Dezayes et al., 1995). They are analogous to the N-striking FIP sets, which are always dominant. In addition, E-striking FIP sets could have been created by local stress switching at the grain scale. Such a phenomenon is not observed at a smaller scale. The absence of mesoscopic counterparts of some FIP sets shows that these sets are specific to the microscopic scale. Then, the network is less scattered at small scale. The weakness induced by FIP at a microscopic scale must be taken into account in mechanical and hydrological modelling. Its effect on permeability may not be negligible.

Acknowledgements

BRGM supported the geological investigations. SOCOMINE provided samples and helpful assistance on the site. The authors are grateful to Prof. Henry Charlesworth (University of Alberta) for commenting on the English and Dr. Anne-Marie Boullier (UMR5559 CNRS, Grenoble) for helpful discussions. Contribution LGCA ESA CNRS 5025 n° 2445.

References

Angelier, J., Bergerat, F., 1983. Systèmes de contrainte et extension intracontinentale. Bulletin de Centre de Recherches Exploration Production Elf-Aquitaine 7, 137–147.

Brun, J.P., Team ECORS, 1991. Crustal-scale structure of the southern Rhinegraben from ECORS-DEKORP seismic reflection data. Geology 19, 758–762.

Clocchiatti, R., 1975. Les inclusions vitreuses des cristaux de quartz. Mémoires Société Géologique de France 122.

Dezayes, C., Villemin, T., Genter, A., Traineau, H., Angelier, J., 1995. Analysis of fractures in boreholes of Hot Dry Rock project at Soultz-sous-Forêts (Rhine graben, France). Scientific Drilling 5, 31–41.

Dubois, M., Ayt Ougougdal, M., Meere, P., Royer, J.-J., Boiron, M.-C., Cathelineau, M., 1996. Temperature of paleo- to modern self-sealing within a continental rift basin: The fluid inclusion data (Soultz-sous-Forêts, Rhine graben, France). European Journal of Mineralogy 8, 1065–1080.

Fisher, N.I., Lewis, T., Embleton, B.J.J., 1987. Statistical Analysis of Spherical Data. Cambridge University Press, Cambridge.

Genter, A., 1989. Géothermie roches chaudes séches: le granite de Soultz-sous-Forêts (Bas-Rhin, France). Fracturation naturelle, altérations hydrothermales et interaction eau-roche. BRGM Document 185, 201 Ph.D. Thesis, University of Orléans.

Genter, A., Traineau, H., 1992. Borehole EPS1, Alsace, France: preliminary geological results from granite core analyses for Hot Dry Rock research. Scientific Drilling 3, 205–214.

Gérard, A., Kappelmayer, O., 1987. The Soultz-sous-Forêts Project. Geothermics 16, 393–399.

Hollister, L.S., Crawford, M.L., Roedder, E.W., Burruss, R.C., Spooner, E.T.C., Turret, J., 1981. Practical aspects of microthermometry. In: Hollister, L.S., Crawford, M.L. (Eds.), Fluid Inclusions, Applications to Petrology. Minerological Association of Canada Short Course Handbook, 6, 278–304.

Kölher, H., 1989. Geochronology on the granite core material from GPK1, Soultz-sous-Forêts. Ruhr Universität, Bochem Report.

Ledésert, B., 1995. Fracturation et paléocirculations hydrothermales. Application au projet de géothermie roches chaudes sèches de Soultz-sous-Forêts (Alsace). Annales de la Société Géologique du Nord T. 4, 13–20.

Lespinasse, M., Pêcher, A., 1986. Microfracturing and regional stress field: a study of the preferred orientations of fluid-inclusion planes in a granite from the Massif Central, France. Journal of Structural Geology 8, 169–180.

Roedder, E. 1979. Fluid inclusions as samples of ore fluids. In: Barnes, H. (Ed.), Geochemistry of Hydrothermal Ore Deposits. Wiley Interscience, New York, p. 798.

Terzaghi, R., 1965. Sources of error in joint surveys. Geotechnique 15, 287–304.

Villemin, T., 1986. La chronologie des événements tectoniques dans le Nord-Ouest de la France et le Sud-Est de l'Allemagne du Permien à l'actuel. Comptes Rendues Academie Sciences Paris 303, 1685–1690.